Structural model, functional modulation by ivermectin and tissue localization of Haemonchus contortus P-glycoprotein-13

Marion David, Chantal Lebrun, Thomas Duguet, Franck Talmont, Robin Beech, Stéphane Orlowski, François André, Roger K. Prichard, Anne Lespine

To cite this version:

Marion David, Chantal Lebrun, Thomas Duguet, Franck Talmont, Robin Beech, et al.. Structural model, functional modulation by ivermectin and tissue localization of Haemonchus contortus P-glycoprotein-13. International journal for parasitology. Drugs and drug resistance, 2018, 8 (1), pp.145–157. 10.1016/j.ijpddr.2018.02.001 . hal-02177610

HAL Id: hal-02177610
https://hal.science/hal-02177610v1

Submitted on 26 May 2020

IJP: Drugs and Drug Resistance 8 (2018) 145–157

Contents lists available at ScienceDirect

IJP: Drugs and Drug Resistance

journal homepage: www.elsevier.com/locate/ijpddr

Structural model, functional modulation by ivermectin and tissue localization of *Haemonchus contortus* P-glycoprotein-13

Marion David[a,b,1], Chantal Lebrun[a,1], Thomas Duguet[b], Franck Talmont[c], Robin Beech[b], Stéphane Orlowski[d], François André[d], Roger K. Prichard[b,**], Anne Lespine[a,*]

[a] *INTHERES, Université de Toulouse, INRA, ENVT, Toulouse, France*
[b] *Institute of Parasitology, McGill University, Sainte-Anne-De-Bellevue, Canada*
[c] *Institute of Pharmacology and Structural Biology, UMR 5089, CNRS, Toulouse, France*
[d] *CEA, Institut de Biologie Frédéric Joliot, Centre de Saclay, SB2SM, UMR9198 CNRS, I2BC; 91191 Gif-sur-Yvette Cedex, France*

ARTICLE INFO

Keywords:
Nematode
Haemonchus contortus
ABC transporters
P-glycoprotein
Ivermectin
Homology modeling

ABSTRACT

Haemonchus contortus, one of the most economically important parasites of small ruminants, has become resistant to the anthelmintic ivermectin. Deciphering the role of P-glycoproteins in ivermectin resistance is desirable for understanding and overcoming this resistance. In the model nematode, *Caenorhabditis elegans,* P-glycoprotein-13 is expressed in the amphids, important neuronal structures for ivermectin activity. We have focused on its ortholog in the parasite, Hco-Pgp-13. A 3D model of Hco-Pgp-13, presenting an open inward-facing conformation, has been constructed by homology with the Cel-Pgp-1 crystal structure. In silico docking calculations predicted high affinity binding of ivermectin and actinomycin D to the inner chamber of the protein. Following *in vitro* expression, we showed that ivermectin and actinomycin D modulated Hco-Pgp-13 ATPase activity with high affinity. Finally, we found *in vivo* Hco-Pgp-13 localization in epithelial, pharyngeal and neuronal tissues. Taken together, these data suggest a role for Hco-Pgp-13 in ivermectin transport, which could contribute to anthelmintic resistance.

1. Introduction

Parasite nematodes cause morbidity in animals and humans and macrocyclic lactones (ML), such as ivermectin (IVM), are important anthelmintic drugs for therapy (Campbell, 2016; Omura, 2016). However, the long-term use of ML has led to the development of drug resistance, challenging therapeutic control (Kaplan and Vidyashankar, 2012).

The multi-drug resistance (MDR) transporters from the ATP-binding cassette (ABC) protein superfamily are involved in the transport of structurally unrelated xenotoxins, and have been recognized as major players in resistance to drugs in mammals, bacteria and parasites (Lage, 2003; Jones and George, 2005; Koenderink et al., 2010). In mammals, P-glycoprotein (MDR1/ABCB1/Pgp) can efflux structurally unrelated drugs, including IVM (Schinkel et al., 1994; Pouliot et al., 1997; Roulet et al., 2003; Lespine et al., 2007). Many Pgps, i.e. full-size transporters of the B sub-family, are expressed in nematodes, and they display fair sequence homologies with human ABCB1. The free-living nematode *Caenorhabditis elegans* expresses sixty ABC proteins, among which fourteen Pgp homologs are localized in different organs and expressed at various stages of development (Zhao et al., 2004). *Haemonchus contortus*, one of the most prevalent pathogen parasitic nematodes in small ruminants, is genetically close to *Caenorhabditis elegans* and its genome has recently been sequenced (Laing et al., 2013) (ftp://ftp.sanger.ac.uk/pub/pathogens/Haemonchus/contortus). In this species, ten homologs of Pgps were identified, and two have been localized: Hco-Pgp-2 in the pharynx, anterior intestine and head neurons, and Hco-Pgp-9.1 in the uterus of females (Godoy et al., 2015a, 2016).

There is indirect but converging evidence that some nematode Pgps can transport ML, in *C. elegans* (Ardelli and Prichard, 2013; Janssen et al., 2013a, 2015) and in *Parascaris equorum* (Janssen et al., 2013b). Some mammalian Pgp inhibitors alter the transport function of Pgps in

---

Abbreviations: ABC, ATP-binding cassette; ACD, actinomycin D; AH, anthelmintic; BlastP, protein Basic Local Alignment Search Tool; bp, base pairs; Cel, *Caenorhabditis elegans*; Hco, *Haemonchus contortus*; Hsa, *Homo sapiens*; IVM, ivermectin; MDR, multidrug resistance; ML, macrocyclic lactone(s); Mmu, *Mus musculus*; NBD, nucleotide binding domain; PDB, Protein data bank; Pgp, P-glycoprotein; QMEAN, Qualitative Model Energy Analysis; RMSD, root mean square deviation; SNP, single nucleotide polymorphism; TM(D), transmembrane (domain)

[*] Corresponding author. INRA-INTHERES_UMR 1436, 180, Chemin de Tournefeuille, BP 93173, F-31027, Toulouse Cedex 3, France.

[**] Corresponding author. Institute of Parasitology, McGill University, Macdonald Campus, 21111, Lakeshore Road, Ste Anne-de-Bellevue, QC, H9X 3V9, Canada.

E-mail addresses: roger.prichard@mcgill.ca (R.K. Prichard), anne.lespine@inra.fr (A. Lespine).

[1] Contributed equally.

https://doi.org/10.1016/j.ijpddr.2018.02.001
Received 31 October 2017; Received in revised form 9 February 2018; Accepted 12 February 2018

C. elegans and in the parasitic nematodes *H. contortus*, *Cylicocylus elongatus* and *Dirofilaria immitis* (Kaschny et al., 2015; Godoy et al., 2015a, 2015b, 2016; Mani et al., 2016). Such inhibitors can also improve the susceptibility of nematodes to ML (Bartley et al., 2009; James and Davey, 2009; Lespine et al., 2012; Menez et al., 2016). In addition, increased ML resistance is associated with induction of expression of Pgp genes (James and Davey 2009; Lespine et al., 2012). Recently, using the first crystal structure of a nematode Pgp, Cel-Pgp-1, resolved at a resolution of 3.4 Å (Protein Data Bank code: 4F4C) (Jin et al., 2012), high affinity binding of several anthelmintic drugs, including IVM, on Cel-Pgp-1 has been predicted by *in silico* docking calculations (David et al., 2016).

To understand the respective physiological functions of Pgps in *H. contortus*, it is of interest to consider their sites of expression. In both *C. elegans* and *H. contortus*, IVM resistance has been linked to defects in the morphology of the amphids (Freeman et al., 2003; Urdaneta-Marquez et al., 2014; Menez et al., 2016). *Cel-Pgp-6* and *Cel-Pgp-13* are expressed in the amphids (Zhao et al., 2004). *H. contortus* does not have a homolog of *Cel-Pgp-6*, but it has a homolog of *Cel-Pgp-13*, and it was therefore of interest to characterize *Hco-Pgp-13*. Full-length *Hco-Pgp-13* cDNA was cloned and transfected into *Pichia pastoris* which stably expressed functional Hco-Pgp-13. Based on the crystal structure 4F4C of Cel-Pgp-1 (Jin et al., 2012), the protein was 3D modeled in open inward-facing conformation, which is expected to be competent for substrate uptake, leading to two high-quality, alternative but complementary, structural models. Using *in silico* docking on these models, in combination with *in vitro* ATPase assays on membranes of *Hco-Pgp-13* transfected *P. pastoris*, we show for the first time that actinomycin D (ACD) and IVM specifically bind to Hco-Pgp-13 and modulate its ATPase activity, and could hence be transported by the parasitic Hco-Pgp-13. Furthermore, the expression of Hco-Pgp-13 in the tissues of *H. contortus* larvae and adults was assessed. Our finding of apparent Hco-Pgp-13 expression in digestive, epithelial and neuronal tissues is consistent with a general detoxification function, possibly handling various xenobiotics, in analogy with ABCB1 in mammals. Finally, in the context of anthelmintic drug resistance in parasitic nematodes, Hco-Pgp13 is likely to have a role in IVM resistance.

2. Material and methods

2.1. Parasites

The PF23 strain of *H. contortus* used is susceptible to MLs (Ranjan et al., 2002). Worms were originally supplied by Fort Dodge Animal Health, Princeton, NJ, USA and were maintained by our laboratory. Animals and standardized operating procedures used in this research study were approved (Protocol 3845) and subjected to the guidelines from the Animal Care Committee of McGill University, Canada. Worms were obtained from passages consisting of an artificial infection with the larvae from the previous generation in naive lambs, without anthelmintic exposure. They were then collected from the abomasum of the host and incubated in PBS at 37 °C before storage at -80 °C.

2.2. RNA extraction and reverse transcription

Total RNA was extracted from twenty adult *H. contortus*, homogenized and extracted according to the instruction of the manufacturer (ThermoFisher, Canada). RNA concentration was determined with a Nanodrop photometer IMPLEN® at a wavelength of 260 nm and assessed by gel electrophoresis. Good quality RNA was stored at -80 °C. The reverse transcription to cDNA was performed using the SuperScript® III reverse transcriptase (ThermoFisher, Canada), starting with 1 µg RNA and following the instructions of the manufacturer. The cDNA obtained was stored at -20 °C for further use.

2.3. Amplification of the Hco-Pgp-13 cDNA sequence

A pair of primers, *Hco-Pgp-13*-F1 and *Hco-Pgp-13*-R2 (Suppl. Table S1), were designed using the Geneious software version 5.5.6. (http://www.geneious.com/; PO Box 5677, Wellesley St, Auckland 1141, New Zealand), across the 3' end of the predicted sequence of *Hco-Pgp-13* from the Sanger Institute (ftp://ftp.sanger.ac.uk/pub/pathogens/Haemonchus/contortus) (Laing et al., 2013). A first PCR was run using these primers and the reverse transcribed cDNA of whole adult *H. contortus* as template. A fragment of 3488bp was obtained and sequenced (Genome Quebec Innovation Centre, McGill University, QC, Canada) using eight primers, *Hco-Pgp-13*-F1 to *Hco-Pgp-13*-R8 (Supplementary Table S1).

Four more primers were designed to identify the 5′-end of *Hco-Pgp-13* by nested PCR: the nematode spliced leader sequence SL1 (Blaxter and Liu, 1996), a specific forward primer *Hco-Pgp-13*–F9 (Supplementary Table S1) and two specific reverse primers *Hco-Pgp-13*–R10 and *Hco-Pgp-13*-R11 (Supplementary Table S1). The 887 bp PCR products thus obtained were sequenced and aligned to the first 3488 bp product with MultAlin software (Corpet, 1988), and the overlap of the amplicons confirmed. The full-length sequence was then aligned against the cDNA of the predicted sequence of *Hco-Pgp-13* using MultAlin (Supplementary Figure S1).

2.4. Determination of Hco-Pgp-13 protein sequence, phylogenic analysis and calculation of TMD homologies relative to Cel-Pgp-1

The translation of *Hco-Pgp-13* cDNA into protein sequence was performed using ExPASy – Translate tool (http://web.expasy.org/translate/). The parameters of the protein (molecular weight, length) were calculated with ExPASy – ProtParam (http://web.expasy.org./protparam/). The presence of N- and O-glycosylation motifs was predicted using ExPASy - ScanProsite tool (http://prosite. Expasy. org/), as well as that of consensus motifs, including the Walker A and the less conserved Walker B motif. Multiple sequence alignment of Pgps of various organisms, including Hsa-Pgp (Supplementary Figure S2), was performed using Muscle algorithm under Seaview software (Edgar, 2004a, 2004b). The prediction of amino acids located within the transmembrane bilayer was performed with the Protter tool (Omasits et al., 2014) and the TMHMM Server v. 2.0 (http://www.cbs.dtu.dk/services/TMHMM/). The visualization of the topology of the full length protein sequence across the plasma membrane was represented using the Protter tool (Fig. 1). The TM helices and eight N-glycosylation motifs were represented as predicted by this program, N518 being the only one not previously predicted by ExPASy - ScanProsite.

A PhyML phylogenetic tree with all Hco-Pgps, all Cel-Pgps, Hsa-Pgp and Mmu-ABCB1a protein sequences (Fig. 2) was constructed using Seaview software from the multiple alignments previously performed with Muscle (Supplementary Figure S2) after removal of NBDs from all the considered protein sequences.

The locations of the TMDs of all the proteins of this alignment were deduced from Cel-Pgp-1 4F4C crystal structure (Jin et al., 2012). The first amino acid of TMD1 of each Pgp was identified as the one aligned to the first amino-acid of TM1 of Cel-Pgp-1, thus excluding the small extra-helix TMa and TMb (Jin et al., 2012) not previously described in other ABC transporters, and considered to be part of the N-terminal region. The similarity and identity percentages of the TMDs of Cel-Pgp-1 with the TMDs of all other Pgps were then determined using BlastP (http://blast.ncbi.nlm. nih. gov/Blast.cgi). TMD1 and TMD2 were considered independently, and the mean of the two values for each Pgp is reported in Table 1.

2.5. Design of specific antibodies against Hco-Pgp-13

The specificity and suitability of various antigens for antibody production against Hco-Pgp-13 were analyzed by GenScript. Among

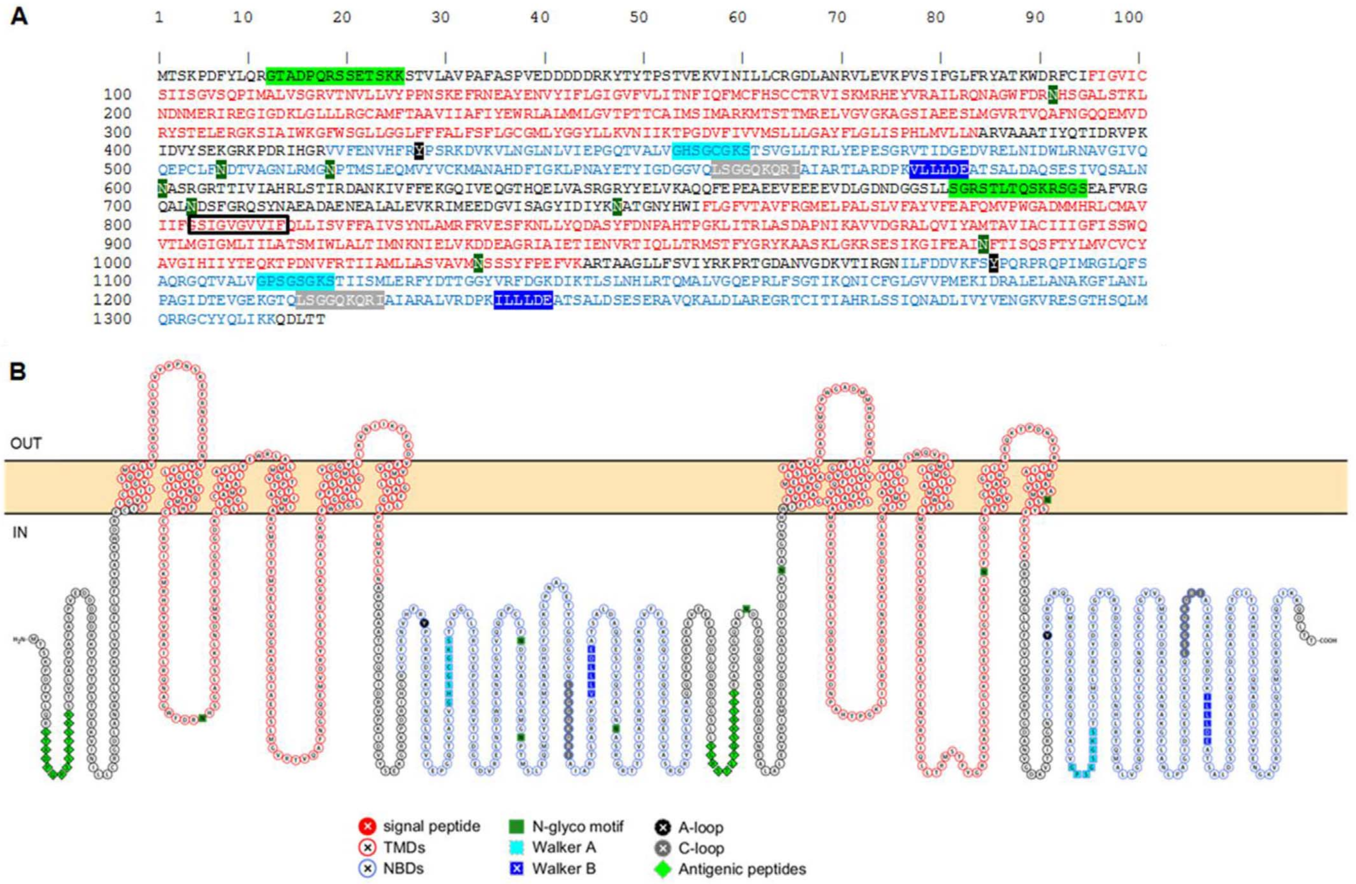

Fig. 1. Primary sequence (A) and predicted topology (B) of Hco-Pgp-13. The amino acid sequence was predicted using ExPASy - Translate, the various motifs were found using ExPASy – ScanProsite, and the topology was represented with Protter. The sequence of transmembrane domains (TMDs), TMD1 (residues 95-383) and TMD2 (residues 756-1043), and nucleotide binding domains (NBDs), NBD1 (residues 418-654) and NBD2 (residues 1076-1312), are colored in red and blue characters, respectively (A), or as cellular topology in red and blue circles, respectively (B). Within each NBD, the Walker A domain sequence is highlighted in light blue and the Walker B motif in dark blue (A and B), in squares (B). The tyrosine residue forming the A-loop of each domain is highlighted in black (A and B), and the C-loop/ABC transporter signature motif is highlighted in grey (A and B); both are circled in (B). Putative N-glycosylation motifs (Asn 191, 507, 518, 601, 704, 747, 984 and 1033) are highlighted in dark green (A and B), in squares (B). Protein regions chosen as antigenic determinant n°1 (N-term region) and n°2 (between NBD1 and TMD2) are both highlighted in light green (A), in diamonds (B). The ten residues sequence within the black box (A) was duplicated in the predicted sequence published by Laing et al. (2013) (See Supplementary Fig. S1). (For interpretation of the references to colour in this figure legend, the reader is referred to the Web version of this article.)

several potential antigenic determinants identified, two peptides were chosen for their disordered structure and high accessibility in the predicted 3D conformation of the protein: GTADPQRSSETSKK (residues 12-25) and SGRSTLTQSKRSGS (residues 681-694). They were chemically synthesized and used to immunize rabbits (GenScript, USA). The polyclonal antibodies generated were assessed in Western blots.

2.6. Expression of Hco-Pgp-13

The full-length cDNA sequence of *Hco-Pgp-13* was subjected to codon optimization by GenScript (NJ, USA). After transformation of the vector in *Escherichia coli* TOP10F' competent cells, *Hco-Pgp-13* codon optimized sequence was confirmed by sequencing (Genome Quebec Innovation Centre, McGill University, QC, Canada). Expression of codon optimized *Hco-Pgp-13* was undertaken in both epithelial pig kidney cells (LLC-PK1) and *P. pastoris*. Membrane fractions extracted from Hco-Pgp-2/LLC-PK1 transfected cells (Godoy et al., 2015a) and from Hco-Pgp-13/LLC-PK1 were prepared as previously described (Garrigues et al., 2002).

For expression in *P. pastoris*, *Hco-Pgp-13* coding sequence was modified at the 5′ end and the 3′ end by introducing BstBI and XbaI sites, respectively, by PCR amplification with the following primers: BstBI-*Hco-Pgp-13*: 5′AAAACAACTTAATTATTATTCGAAACGATGACATCAAAACCCGAT′3 (forward) and XbaI-*Hco-Pgp-13*: 5′TAGCTAGCTAGCTAGCTAGTGTTCTAGAGGCCCTGTGGTGAGG TCCTGC′3 (reverse). Modified PCR cDNA was digested using BstBI and XbaI enzymes and cloned in the pPICZ-HuMOR-cmyc-his-tag vector (Sarramegna et al., 2005) digested with the same enzymes leading to the creation of pPICZ-Hco-Pgp-13-cmyc-his-tag vector.

E. coli strain Top10F' was used for the propagation of recombinant plasmids. *E. coli* transformants were selected on low salt LB plates pH 7.5 (0.5% w/v yeast extract, 1% w/v tryptone, 0.5% w/v NaCl, 1.5% w/v bacteriological agar) supplemented with 25 μg zeocin/ml. *P. pastoris* SMD1163 (his4, pep4, prB1) strain was used for protein expression. Transformants were selected on YPDS plates (1% w/v yeast extract, 2% w/v peptone, 2% w/v dextrose, 1 M sorbitol, and 1.5% w/v bacteriological agar) with 100 μg zeocin/ml. *P. pastoris* growth and induction were performed in BMGY medium (1% w/v yeast extract, 2% w/v peptone, 0.1 M phosphate buffer pH 7.5, 1% v/v glycerol) and BMMY medium (same as BMGY except that glycerol was replaced by 0.5% v/v methanol), respectively. For some experiments growth and recombinant protein expression were undertaken at the same time in BMMY medium. Cell cultures were conducted at 30 °C in shacking flasks.

2.7. Cell membrane preparation and western blot

P. pastoris and LLC-PK1 cells were harvested and ruptured during

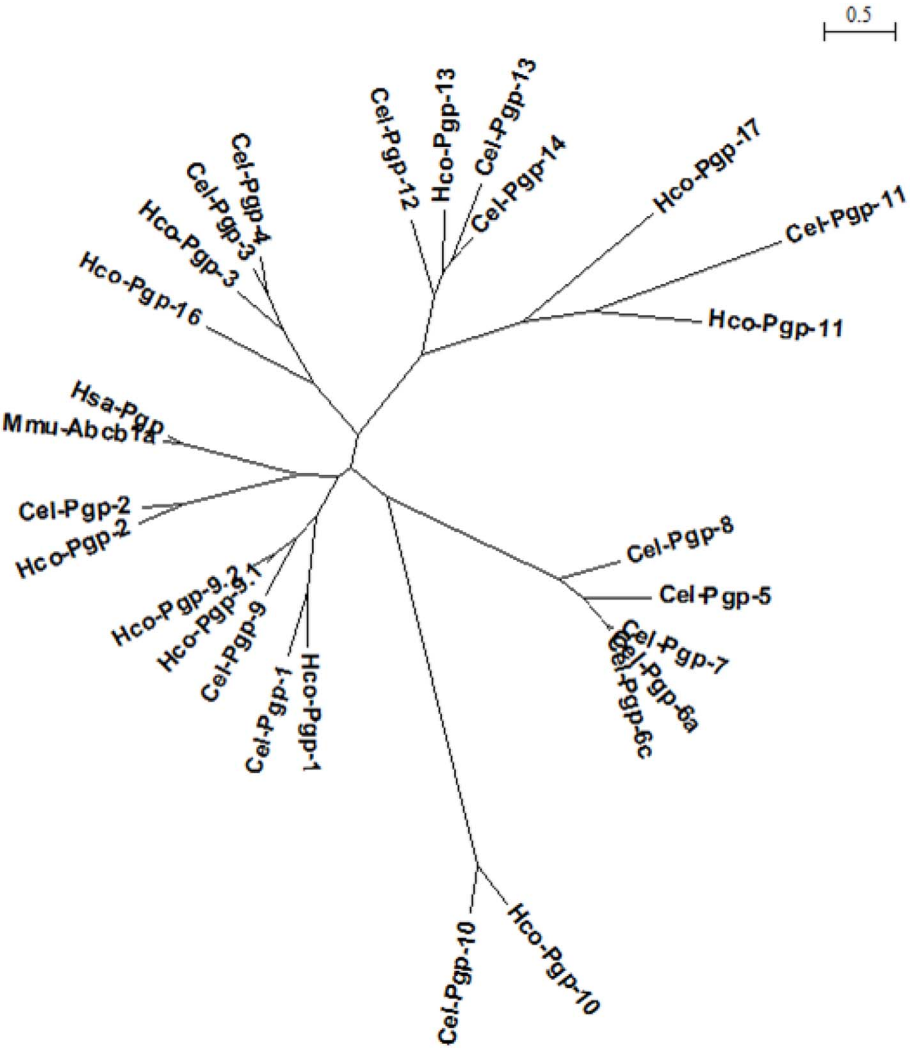

Fig. 2. Maximum likelihood phylogenetic tree of mammalian and nematode Pgp protein sequences. A PhyML phylogenetic tree of a set of sequences comprising Hco-Pgps, Cel-Pgps, Hsa-ABCB1 and Mmu-ABCB1a protein sequences, with their NBD regions removed, was built using Seaview software, based on the Muscle alignment shown in Supplementary Figure S2. The bar represents the relative scale of distance, expressed in number of substitutions per site of the sequence alignment.

30 min with glass beads, or by sonication, in buffer (Tris/HCl 10 mM, pH 7.5) supplemented with protease inhibitors, at 4 °C. The cell lysate was centrifuged at 1,000g for 15 min to remove particulate matter. The supernatant was then centrifuged at 100,000g for 30 min. Resulting pellets were stored at -80 °C in the same buffer. Membrane protein content was determined using the Bradford assay (Bio-Rad), using bovine serum albumin (BSA) as standard.

SDS-PAGE and transfer to nitrocellulose were performed as described (Gallagher, 2016). The primary anti-His tag antibody (Thermo Scientific) was diluted 1:1000 as well as the two primary antibodies designed against each epitope of Hco-Pgp-13. The secondary CF™770 anti-rabbit antibody (Biotium, Fremont, CA, USA) was used at a 1:10000 dilution. Detection was carried out using the Odyssey® CLx imaging system (LI-COR Biosciences, Lincoln, NE, USA).

2.8. ATPase activity measurements

The vanadate-sensitive ATPase activity of freshly prepared crude membranes from *P. pastoris* cells transformed by pPICZ-Hco-Pgp-13-cmyc-his-tag vector (Hco-Pgp-13: three membrane preparations) were compared to *P. pastoris* cells transformed by pPICZ-HuMOR-cmyc-his-tag vector (Sarramegna et al., 2005) (Hu-MOR: two membrane preparations) as negative controls and to untransfected *P. pastoris* cells (WT: three membrane preparations). The ATPase activity was measured at 37 °C by the endpoint inorganic phosphate (Pi) release assay (Sarkadi et al., 1992). Briefly, membrane preparations (200 µg/ml) were preincubated at 37 °C in ATPase assay buffer (50 mM HEPES (pH 7.5), 10 mM $MgCl_2$, 1 mM dithiothreitol, 0.1 mM EGTA, 10 mM sodium azide, 1 mM ouabain) in the presence or absence of 100 µM sodium orthovanadate and with increasing concentrations of either ACD or IVM. DMSO (final concentration was 1%) was used as solvent for the drugs and in the control measurements. The reaction was initiated by the addition of 5 mM ATP and stopped with 5% SDS solution after 5, 15 and 30 min of incubation. The amount of Pi released was determined at each time point in triplicate and the mean initial hydrolysis rate was calculated in nmol Pi/min/mg of total membrane protein (+/- SD). The vanadate sensitive activity values were estimated as the difference between the rate in the presence and absence of vanadate. For studying ACD-induced ATPase, in each of the different membrane preparations, data were normalized to 100% with respect to the vanadate-sensitive activity measured in the absence of added drug. For studying IVM modulation of ATPase activity data are presented as absolute values. In order to quantitatively analyze the interaction of ACD and IVM with Hco-Pgp-13, we assumed that these ligands have one specific site (or indepemdent sites) on the protein, and fitting was carried out using non-linear regression with GraphPad PRISM.

Table 1
Percentage of amino acid identity and similarity of TMD1-TMD2 domains of various Pgps relative to Cel-Pgp-1, as given by BlastP. The TMDs were extracted according to the multiple sequence alignments generated by Muscle, as shown in Suppl. Fig. S2. For each Pgp, TMD1 and TMD2 were determined by alignment with Cel-Pgp-1 TMDs as given by the 4F4C crystal structure (Jin et al., 2012). TMD1 was considered as starting at TM1 of 4F4C, thus excluding the TMa-b transmembrane hairpin not described in other known ABC transporter structures. Each TMD homology was calculated independently, and the mean of the two values is reported. **Bold**: Cel-Pgps and Hco-Pgps showing a long N-terminal sequence (>70 AAs). The list is displayed in decreasing order of similarity. ND: not determined as Cel-Pgp-10 presents a longer TMD1 than other Pgps.

Cel-Pgp-1	% Identity	% Similarity
Hco-Pgp-1	63	79
Hco-Pgp-9.1	50	69
Cel-Pgp-9	48	67
Hsa-Pgp	36	58
Cel-Pgp-2	35	57
Mmu-Abcb1a	35	56
Hco-Pgp-2	34	56
Hco-Pgp-13	**33**	**54**
Hco-Pgp-16	32	52
Cel-Pgp-3	30	52
Hco-Pgp-3	31	51
Cel-Pgp-4	30	51
Cel-Pgp-8	29	51
Cel-Pgp-12	**28**	**51**
Hco-Pgp-17	25	51
Cel-Pgp-5	30	50
Cel-Pgp-14	**29**	**50**
Cel-Pgp-13	**27**	**50**
Cel-Pgp-7	29	49
Cel-Pgp-6a	29	49
Hco-Pgp-11	25	46
Cel-Pgp-11	**22**	**45**
Hco-Pgp-10	**22**	**42**
Cel-Pgp-10	**ND**	**ND**

2.9. Construction of 3D models of Hco-Pgp-13 and in silico docking calculations

All Modeller and Autodock calculations were performed using the computing facilities of the CEA-DSV/GIPSI (cluster Gabriel) at Saclay, France and of INRA (Genotoul) in Toulouse, France. 3D models of Hco-Pgp-13 were built using Modeller 9v12 (Sali and Blundell, 1993; Webb and Sali, 2014) based on the crystal structure of *C. elegans* Pgp-1 (PDB: 4F4C, determined at a resolution of 3.4 Å), as a template (Jin et al., 2012). As the Cel-Pgp-1 sequence was lacking the following amino acids: M1-R3, A52-E54, K666-E715 and G1307-K1321, the full-length sequence of Hco-Pgp-13 was modeled without the corresponding aligned residues: M1-S3, E668-L725, and G1304-T1317. The pairwise alignment was deduced from the multiple alignment (Supplementary Figure S2) in order to improve the accuracy of the homology modeling alignment used as input for Modeller 9v12. Then, 100 models were generated in each Modeller run, and they were ranked according to their DOPE (Discrete Optimized Protein Energy) score and their molecular PDF value of the optimized objective function of Modeller. The best DOPE score model, n°4 (Hco-Pgp-13_04), and the best molecular PDF model, n°52 (Hco-Pgp-13_52), were submitted to various online servers to assess their protein structure quality (Supplementary Table S2). The QMEAN (Qualitative Model Energy Analysis) scoring function (Benkert et al., 2008, 2009), the ProSA-web (Protein structure analysis) (Sippl, 1993; Wiederstein and Sippl, 2007) and the VADAR (Volume, Area, Dihedral Angle Reporter) (Willard et al., 2003) servers all indicated very close assessment for the two models according to different parameters, so that both of them were retained for docking calculations.

The *in silico* docking calculations for ACD and IVM on Hco-Pgp-13 were performed as previously described (David et al., 2016). The structure of ACD was extracted from DrugBank n° DB00970 and the structure of IVM was extracted from the Merck Index (https://www.rsc.org:merck-index). For both molecules, 10 minimum energy conformers were generated with Marvin Suite under the MMFF94 force field (https://www.chemaxon.com/products/marvin/marvinsketch/). After 3D-alignment and calculation of RMSD under PyMOL four representative conformers were chosen for starting the docking calculations. Molecular docking experiments were performed using AutoDock 4 (release 4.2.6) in the semi-flexible mode, with the Hco-Pgp-13_04 and Hco-Pgp-13_52 PDB structures kept rigid, and prepared with AutoDock Tools (Morris et al., 1998, 2009). The grid built by AutoGrid 4 included 95, 120, and 100 points in x, y, and z directions, with a grid spacing of 0.375 Å, to allow a good compromise between resolution of the explored volume and the size of the binding area (box dimensions 35.6 × 45.0 × 37.5 Å, centered in the inner cavity of Hco-Pgp-13 at the point x = 23 Å; y = 78 Å; z = -2 Å). For each ligand conformer, 100 runs were performed using the Lamarckian genetic algorithm. All the other parameters were set at the default value. The 100 generated poses were assigned a score calculated by AutoDock that can be considered as an estimated free energy of ligand binding (indicative of binding affinity). They were then clustered as a function of the closeness of their positions and conformations, with RMSD set at 2.0 Å, and finally ranked by their binding score (determined for the best pose in the cluster). For each lowest energy pose of selected clusters, the number and nature of interacting residues were analyzed within the protein. Among these, particular interest was given to residues belonging to the "hotspots for drug binding". These are a collection of 62 residues, as displayed in Supplementary Table S3, coming from different experimental approaches that have been conducted for the purpose of determining the key residues responsible for multidrug recognition by mammalian Pgp (Hsa-ABCB1, Mmu-ABCB1a, Mmu-ABCB1b, Cgr-ABCB1) (Loo and Clarke, 2001, 2002; Shilling et al., 2006; Loo et al., 2006a, 2006b; Aller et al., 2009; Bessadok et al., 2011; Li et al., 2013). All these residues are situated in the transmembrane part of the protein, and 14 of these 62 residues are common between at least two different approaches. Altogether, they provide a frame in the inner chamber that offers a set of anchor points for multi-specific recognition and binding, and eventual translocation, of various transport ligands. Multiple protein sequence alignments have been performed on Hco-Pgp-13, Cel-Pgp-1, human ABCB1, murine ABCB1a and B1b, and Chinese hamster ABCB1, using Muscle software (Edgar, 2004a), to identify the corresponding residues in Hco-Pgp-13.

2.10. Immunohistochemistry on larvae and adult H. contortus cryosections

The anti-Hco-Pgp-13 antibodies validated in Western-blot were used for immunohistofluorescence detection of Hco-Pgp-13 protein in L3 larvae and adult *H. contortus*. An anti-myosin antibody directed against *C. elegans* myosin heavy chain A was also used to localize muscles (product 5-6 of Developmental Studies Hybridoma Bank, University of Iowa, IA, USA). Fresh worms were fixed in 4% PFA in PBS at 4 °C for 16 h. They were then washed and incubated in 30% sucrose in PBS at 4 °C for 16 h. Whole worms were individually embedded in an optimal cutting temperature compound (OCT) (Thermo Fisher Scientific, Waltham, MA, USA), they were quickly frozen to -80 °C and stored. Cryosections were performed by slicing 20-30 µm thick transverse sections with a Thermo Shandon cryotome (Thermo Fisher Scientific) and slices were collected onto poly-L-lysine coated glass coverslips (Sigma, USA), and kept at -80 °C before further processing.

Sections were incubated in Antibody Diluent (AbD) (PBS, 0.2% gelatin fish skin, 0.1% sodium azide, 0.1% v/v Triton X-100) at 4 °C for 16 h, followed by incubation with the two primary antibodies: anti-myosin and anti-Hco-Pgp-13 with 1/100 and 1/50 dilutions, respectively, in AbD at 4 °C for 16 h. Five washes for 5 min with AbD were performed and the secondary fluorescent antibodies (Alexa Fluor 488-labelled fragment of goat anti-rabbit IgG and Alexa Fluor 635 goat anti-mouse IgG (Invitrogen, USA) were incubated at a 1/500 dilution at 4 °C for 16 h. Sections were washed three times for 5min with AbD and then PBS, mounted on slides using mounting medium (Sigma, Saint Louis, MO, USA) and observed under a fluorescent microscope. The most representative cross-sections were finally 3D analyzed under a confocal microscope (Leica SP8 DMI6000, Wetzlar, Germany) at excitation and emission wavelength of 488/520 nm, respectively for Alexa Fluor 488, and 635/650 nm, respectively, for AlexaFluor 635.

3. Results

3.1. The Hco-Pgp-13 corrected cDNA sequence encodes a protein matching the topology of an ABC transporter with high sequence similarity with Cel-Pgp-12, Cel-Pgp-13 and Cel-Pgp-14

RNA was extracted from adult male and female *H. contortus*, reverse transcribed into cDNA and amplified. Several primers (Supplementary Table S1) were designed along the predicted sequence of *Hco-Pgp-13* (ftp://ftp.sanger.ac.uk/pub/pathogens/Haemonchus/contortus) (Laing et al., 2013). The full sequence obtained, named *Hco-Pgp-13,* corresponds to a 3954 base pairs (bp) coding cDNA from the ATG start codon to the TGA stop codon (Supplementary Figure S1) and is representative of the transcript RNA present in the parasitic worms (GenBank No. KX844966). Compared to the gene sequence previously published (Laing et al., 2013), the alignment data revealed a deletion of 30 nucleotides in the amplified cDNA sequence, which strictly matched a 30-nucleotide repeat present in the *Hco-Pgp-13* sequence predicted in the published genome (Supplementary Figure S1). We deduced that this was due to a misalignment of contigs in the genomic sequencing. In addition, 90 single nucleotide polymorphisms (SNPs) were found over the full length amplified cDNA, which represents 2.3% of the nucleotide sequence (Supplementary Figure S1).

The deduced amino acid sequence of Hco-Pgp-13 contains 1317 residues, and corresponds to an expected molecular weight of 145.9 kDa. It contains eight N-glycosylation motifs, without putative O-glycosylation sites or signal peptide (Fig. 1). It is predicted to possess four structural domains with two hydrophobic transmembrane domains (TMD) and two cytoplasmic domains. The predicted motifs in the nucleotide binding domains (NBD) correspond to ABC transporter family signature motifs (Hewitt and Lehner, 2003) LSGGQKQRI (residues 557–565) in NBD1, and LSGGQKQRI (residues 1215–1223) in NBD2. Aromatic residues (Y427 and Y1085) were found located 25 amino acids upstream of each Walker A motif. These conserved motifs, involved in the hydrolysis of ATP, are consistent with a functional, primary active transporter.

A multiple sequence alignment was performed with all Hco-Pgps, all Cel-Pgps and two mammalian Pgps: Hsa-Pgp and Mmu-ABCB1a, after exclusion of the highly conserved NBDs (Supplementary Figure S2). A phylogenetic tree (Fig. 2) shows that with and without NBDs, (Laing et al., 2013), Hco-Pgp-13 displays a very high degree of homology to Cel-Pgp-12, Cel-Pgp-13 and Cel-Pgp-14, which thus all three appear to be orthologs of Hco-Pgp-13.

3.2. Tertiary structure of Hco-Pgp-13 was generated by homology modeling to Cel-Pgp-1

Since Cel-Pgp-1 is the only crystallographic structure of a nematode Pgp (Protein Data Bank: 4F4C), the homologies of Cel-Pgp-1 TMDs sequences with the TMDs sequences of all other aligned Pgps (Supplementary Figure S2) were calculated using BlastP (Table 1). As expected, Cel-Pgp-1 presented the highest homology for TMDs to Hco-Pgp-1, with 63% identity and 79% similarity of residues, followed by Cel-Pgp-9 and Hco-Pgp-9. Interestingly, N-terminal regions, in the multiple alignment, showed a sequence which extends to 70-90 amino acids for Hco-Pgp-10, Hco-Pgp-13, Cel-Pgp-1, Cel-Pgp-10, Cel-Pgp-11, Cel-Pgp-12, Cel-Pgp-13 and Cel-Pgp-14, against 30-50 amino acids for the nineteen other Pgp sequences aligned, including Hco-Pgp-1 (Table 1, bold, and Supplementary Figure S2). In the crystal structure of Cel-Pgp-1, a transmembrane hairpin (TMa-b, Supplementary Figure S3) was found in the N-terminal region (Jin et al., 2012). Among the Pgps harboring this long N-terminal region (bold, Table 1), Hco-Pgp-13 TMDs showed the highest degree of homology to Cel-Pgp-1 TMDs, with 33% identity and 54% similarity. In contrast, the only other Pgp sequence of *H. contortus* harboring a long N-terminal region, Hco-Pgp-10, only showed 22% identity and 42% similarity to Cel-Pgp-1 TMDs.

The Cel-Pgp-1 4F4C crystal structure was used as a template for building 3D homology models of Hco-Pgp-13, according to the pairwise alignment shown in Supplementary Figure S3. Two models, Hco-Pgp-13_04 and Hco-Pgp-13_52, showed the highest accuracy and very similar scores for quality evaluation (Supplementary Table S2). The open inward-facing conformations of these two high quality models (Supplementary Figure S4) were substantially superimposed. Closer inspection of TMDs of both models showed transmembrane (TM) helices aligned with Cel-Pgp-1 alpha helices, including the small hairpin formed by the N-terminal regions, with a slight shift of their backbones. The TM1 helix and the extracellular loop 1 (ECL1) were found to be shorter in Hco-Pgp-13 than in Cel-Pgp-1 (Supplementary Figure S4B).

When comparing the two Hco-Pgp-13 models, a difference was found in the middle of TM11, where the alpha helix is discontinued only in Hco-Pgp-13_04. At the core of the TMDs, the orientation of the side chains of residues varied between the two models from being almost superimposed (e.g., L366) to pointing in opposite directions (e.g., L1026) (Supplementary Figure S4C).

Interestingly, amino acids of these two Hco-Pgp-13 models, which aligned with those experimentally found to interact with substrates in mammalian Pgps (called “hotspot residues”) (Supplementary Table S3), were mostly found (80%) to point towards the inner chamber formed by the 12 TM helices, thus in an orientation favorable for interaction with potential substrates.

3.3. Hco-Pgp-13 shows in silico high affinity binding sites for ACD and IVM

In order to obtain insights into the functioning of Hco-Pgp-13, we studied, using *in silico* docking on the two structural models, the ability of the protein to interact with two key ligands: ACD, a well-established substrate of mammalian Pgp and Cel-Pgp-1, and IVM, which is the most important anthelmintic used to control parasitic nematodes.

For ACD, the two lowest energy clusters obtained from the docking calculations showed very good binding energies; -16.0 kcal/mol and -14.4 kcal/mol for the Hco-Pgp-13_04 and Hco-Pgp-13_52 models, respectively (Table 2); such energy scores are considered to indicate very high affinity for ligand-protein interaction (Morris et al., 1998, 2009). The binding location of ACD was very close in the two models, occupying the inner chamber of Hco-Pgp-13 from its cytoplasmic opening to its inner core (Fig. 3A and B). These two models of ACD binding showed a similar number of interacting residues: 20 with Hco-Pgp-13_04 model (including 11 hotspot residues) and 19 with Hco-Pgp-13_52 (including 9 hotspot residues). Twelve predicted interacting residues, among which 7 hotspot residues, were common between the two models, with some similarly oriented (e.g., E21, L365, T369) but most of them pointing towards different orientations (e.g. Q108, M916, M995, M1032, N1033) (Fig. 3C and D and Table 2). These differences would explain the different lowest energy positions for ACD in the two models, with different H-bonds formed. For example, Q108, which formed an H-bond with Hco-Pgp-13_04 model, but not with Hco-Pgp-13_52, had a very different orientation in the two models. In contrast, T369 formed an H-bond with Hco-Pgp-13_52 but not with Hco-Pgp-13_04, despite similar orientations. Two H-bonds were formed in both cases, and one of them, formed with N1033, was common between the two models (Fig. 3C and D and Table 2). All three H-bond forming residues were hotspot residues, underlining their importance in substrate binding across species. The role of the small hairpin formed by TMa-b was also significant, as three residues from TMb, i.e. E21, K25 and L29, participated in the stability of ACD on this site in both models (Fig. 3C and D and Table 2). These results indicate a very high affinity of ACD for Hco-

Table 2

Docking characteristics and list of interacting residues of actinomycin D and ivermectin in the Hco-Pgp-13 structure. The parameters and interacting residues listed in column 1 stand for the lowest energy cluster of ACD on Hco-Pgp-13_04 (column 2) and Hco-Pgp-13_52 (column 3), and of IVM on Hco-Pgp-13_04 (column 4) and Hco-Pgp-13_52 (column 5). X: contact residues; X: hotspot residues. **H**: residues establishing a hydrogen bond.

Legend for docking features: a) Number of poses: number of poses in the lowest energy cluster of histogram of poses clustered at rmsd = 2 Å. b) Binding energy (kcal/mol): the energy score calculated by Autodock 4.2. c) Interacting residues: number of contact residues as determined by AutoDock Tools graphical interface. d) Hotspot residues: number of contact residues identified as hotspot residues according to our determination listed in Table S3. e) Hydrogen bonds: number of H-bonds identified by AutoDock Tools between the docked ligands and the protein receptor.

Molecule	**Actinomycin D**		**Ivermectin**	
Hco-Pgp-13 model	04	52	04	52
Docking characteristics				
Number of poses	21	42	19	17
Binding energy (kcal/mol)	-16.0	-14.4	-11.2	-12.8
Interacting residues	20	19	14	21
Hotspot residues	11	9	5	14
Hydrogen bonds	2	2	2	2
Interacting residues				
R11	X			
S19	X		**H**	
S20				X
E21	X	X	**H**	X
K25	X	X		
L29	X	X		
Q108	**H**	X		
S115				X
V118				X
L217	X			
R220		X		
F358				X
M362				X
L365	X	X	X	X
L366		X		
Y369	X	**H**	X	
L373		X	X	
H377	X	X	X	
L772				X
F776				X
L912	X			X
A913				X
M916	X	X	X	X
I917			X	
L919	X	X	X	
A920		X	X	
L921	X		X	
Q989	X			
T992	X			
M995	X	X		X
Y1000				X
F1018				X
L1025				X
L1026				X
S1028				**H**
V1029		X	X	X
V1031				X
M1032	X	X	X	**H**
N1033	**H**	**H**		
S1035		X	X	
S1036	X			
P1039		X		

Pgp-13 with a very close binding site in the two models, located in the cytoplasmic opening of the inner chamber, and thus not much dependent on the orientation of partially flexible residues composing the TMDs.

For IVM, the docking calculations, performed on each model of Hco-Pgp-13, showed close lowest energy clusters, -11.2 kcal/mol and -12.8 kcal/mol for the Hco-Pgp-13_04 model and the Hco-Pgp-13_52 model, respectively, indicating high affinity binding in both cases (Table 2). The binding location of IVM on the Hco-Pgp-13_04 model was close to the cytoplasmic opening of the chamber (Fig. 3A), whereas the binding site of IVM on Hco-Pgp-13_52 was in the deepest part of the inner chamber of the protein (Fig. 3B). These binding positions interacted with 14 residues on model Hco-Pgp-13_04, and 21 residues on model Hco-Pgp-13_52, including 4 hotspots and formed 2 H-bonds on Hco-Pgp-13_04, and 14 hotspots and no H-bonds on Hco-Pgp-13_52 (Fig. 3E and F and Table 2). Thus the binding locations found on the two models were different, with only 5 common residues and with different H-bonds formed: S19 and E21 on Hco-Pgp-13_04, and V1029 and M1032 on Hco-Pgp-13_52 (Fig. 3E and F and Table 2). The binding site of IVM on Hco-Pgp-13 thus appears dependent on the orientation of amino-acids lining the binding chamber. For the Hco-Pgp-13_04 model, it mostly superimposed with the binding site of ACD; the two molecules sharing 9 common interacting residues, including 3 hotspots residues, whereas on Hco-Pgp-13_52, the binding sites of IVM and ACD only superimposed each other at their extremities; nonetheless sharing 6 interacting residues, including 4 hotspots residues.

From this analysis, it can be predicted that both ACD and IVM specifically interact with Hco-Pgp-13 with high affinity at partially overlapping locations within the inner chamber formed by the TMDs. Consequently, these data predict competitive binding of these two ligands on Hco-Pgp-13.

3.4. *Hco-Pgp-13 is functionally expressed in transfected P. pastoris cells*

The ability of Hco-Pgp-13 to interact with ACD and IVM was also studied by analyzing modulation of its ATPase activity. We transfected *P. pastoris* cells with the pPICZ-*Hco-Pgp-13*-cmyc-his-tag vector. The relative expression of Hco-Pgp-13 in the transfected cells was checked by Western blot using an antibody anti-His tag and two specific antibodies. To generate specific antibodies, two antigenic peptides were designed to be specific to Hco-Pgp-13, compared to other *H. contortus* Pgps. When proteins of crude membrane were analyzed by Western-blot, only the 130-kDa protein, otherwise detected with an anti-His tag antibody (Supplementary Figure S5A) reacted with each antibody, showing that the two epitopes were antigenic (Supplementary Figure S5B and C) and confirming that Hco-Pgp-13 was well expressed in the membrane of the transfected *P. pastoris*. The anti-Hco-Pgp-13 antibodies did not give any signal with untransfected mammalian LLCPK1 cells or untransfected *P. pastoris* cells, while the Hco-Pgp-13 transfected cells gave a strong signal to the anti-Hco-Pgp-13 antibodies (Supplementary Figure S5A, B, C). To confirm that the anti-Hco-Pgp-13 antibodies were specific, we checked for any cross reaction with Hco-Pgp-2 and found no cross reactivity (Supplementary Figure S5D, E).

We found that *P. pastoris* membranes from cells expressing Hco-Pgp-13 displayed a higher vanadate-sensitive ATPase activity (150 ± 18 nmol/min/mg) compared to *P. pastoris* cells transfected with pPICZ-HuMOR-cmyc-his-tag vector, used as control (95 ± 5 nmol/min/mg), showing that Hco-Pgp-13 displays a basal ATPase activity (55 ± 23 nmol/min/mg) in the absence of any exogenous compound.

3.5. *Hco-Pgp-13 ATPase activity is modulated by ACD and IVM*

ACD stimulated vanadate-sensitive ATPase activity in Hco-Pgp-13 expressing *P. pastoris* membranes, in a concentration dependent manner with a biphasic profile (Fig. 4A). An activity enhancement of about 1.6-fold and a half-activating concentration around 0.6–1 μM (EC50) were

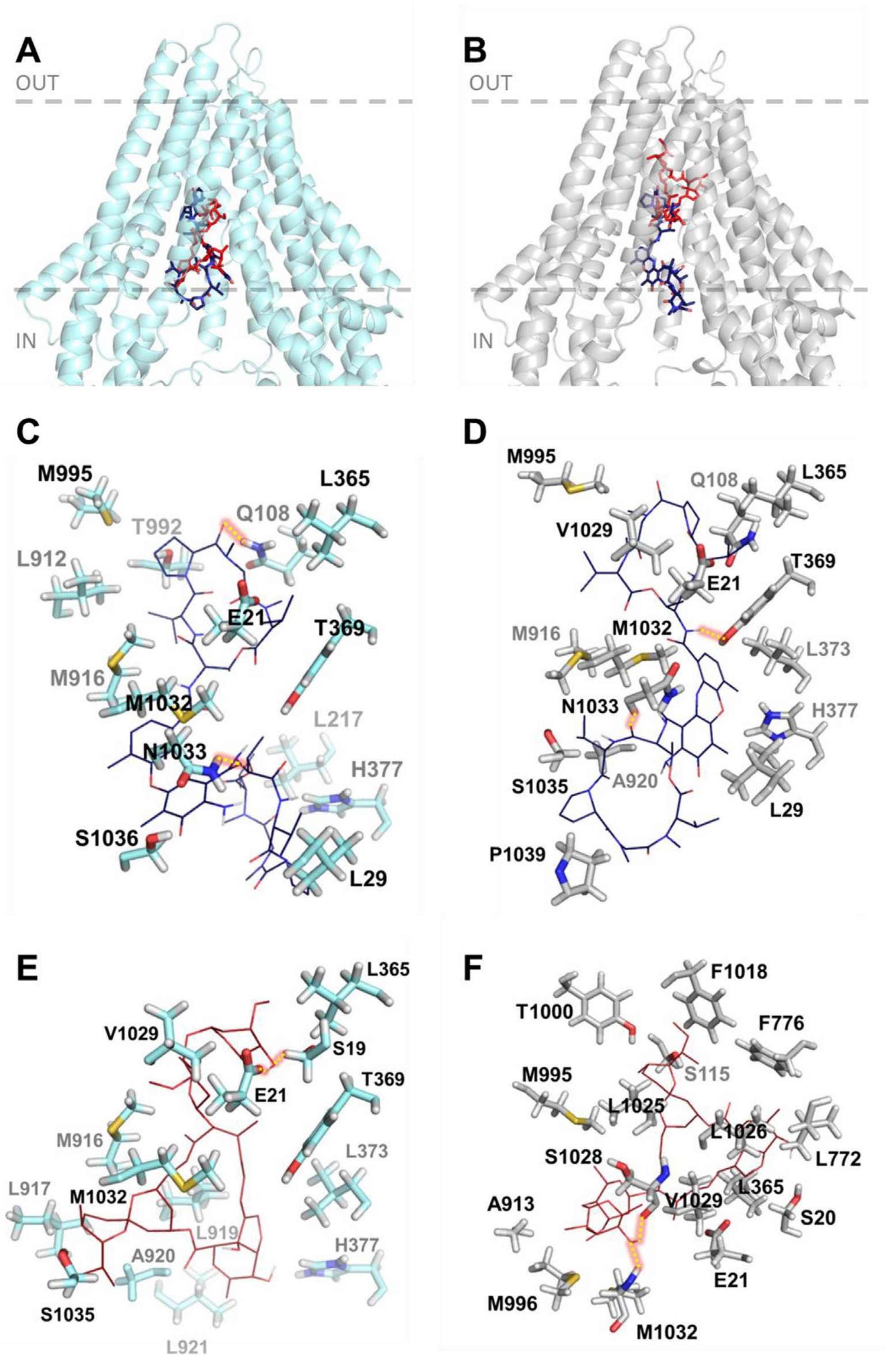

Fig. 3. ***In silico*** **binding of actinomycin D and ivermectin to Hco-Pgp-13 model 04 (A, C, E) and model 52 (B, D, F).** **A** and **B**: Binding sites of the 1st lowest energy clusters of ACD (ACD1) (panel A) and IVM (IVM1) (panel B) on each protein structure resulting from AutoDock 4 calculations. The two molecules are represented together within each of the models of Hco-Pgp-13: 04 (A) and 52 (B). **C-F**: View of the interacting residues of Hco-Pgp-13_04 (**C** and **E**) and Hco-Pgp-13_52 (**D** and **F**) with ACD (**C** and **D**) or IVM (**E** and **F**). Hco-Pgp-13_04 is represented in light blue ribbon and Hco-Pgp-13_52 in grey ribbon. ACD is represented in dark blue sticks (**A** and **B**) or lines in atom type colour mode (**C** and **D**). IVM is represented in red sticks (**A** and **B**) or lines in atom type colour mode (**E** and **F**). Interacting residues of both Hco-Pgp-13 models are represented in sticks in atom type colour mode. All images were generated using PyMol. (For interpretation of the references to colour in this figure legend, the reader is referred to the Web version of this article.)

observed. In contrast, IVM specifically inhibited the basal ATPase activity of Hco-Pgp-13 with a concentration-dependent response curve (Fig. 4B). The concentration giving 50% of the maximal inhibition (IC50) was around 0.5–0.7 μM. In addition, we observed on Hco-Pgp-13 containing membranes, that the ACD-dependent ATPase stimulation was completely inhibited in the presence of 5 μM of IVM (Fig. 4A).

In contrast, in membranes from *P. pastoris* control cells expressing HuMOR, as well as in the membranes from non-transfected *P. pastoris,* the activity was neither activated by ACD nor inhibited by IVM up to 10 μM (Fig. 4A and B). The slight inhibiting effect observed at 10-20 μM is likely attributable to non-specific membrane perturbing effect, which could also explain the small activity decrease observed at 20 μM ACD on Hco-Pgp-13 containing membranes (Fig. 4A and B). Globally, these ATPase modulations strongly indicate that ACD and IVM bind specifically to Hco-Pgp-13 with sub-micromolar apparent affinity.

3.6. Hco-Pgp-13 is expressed in H. contortus digestive, neuronal and epithelial tissues

Given that Hco-Pgp-13 appears likely to be a functional transporter that interacts with IVM and hence possibly plays a role in modulating IVM levels in nematode tissues, it was of interest to determine the expression sites of Hco-Pgp-13. The two anti-Hco-Pgp-13 antibodies were used as a mixture in immunofluorescence assays on transverse cryosections of larvae and adult parasites. In larvae, the Hco-Pgp-13 expression was found in the seam cell between muscle quadrants and more generally in the hypodermis around muscles, including dense bodies between myosin filaments (grey and white arrows, Fig. 5A, panels I and II). Significant staining was also observed at epithelial cells membranes of developing internal organs, corresponding to the gonad or intestine, which could not be readily distinguished at this stage of development (yellow arrow, Fig. 5A, panel II).

In the adult *H. contortus*, Hco-Pgp-13 signal was also found in seam cells-excretory cells, between muscle quadrants and in the surrounding hypodermis (grey and white arrows, Fig. 5B, panels I-IV), as well as at the surface of the male gonad (yellow arrow, Fig. 5B, panel I). In adults, some staining also appeared in the pharynx procorpus at the level of pharyngeal nerve cords that contain cell bodies of epithelial cells, longitudinal extensions of neurons and pharyngeal gland cell processes (purple arrows, Fig. 5B panel II). The staining observed in the metacorpus and terminal bulb also matches the extensions or cell bodies of pharyngeal neurons and gland cells (purple arrows, Fig. 5B, panels III and IV). Additional staining appeared in the head sections between the pharynx and seam cells (blue arrows, Fig. 5B panels III and IV), and within the structure localized at the level of seam cells in other sections (blue arrows, Fig. 5B, panel II). This corresponds to the location of amphidial neurons. Indeed, their dendrites run parallel to the pharynx from the nerve ring to the tip of the head, where seam cells end, and correspond to the amphids. Overall, this broad protein localization matches several organs of the digestive, neuronal, excretory and epithelial systems, suggesting an important physiological role for Hco-Pgp-13.

4. Discussion

There is evidence Pgp efflux pumps play a role in ML resistance in nematodes. Since there is limited structural and functional information on ABC transporters in parasitic nematodes, examining Pgps from *H. contortus*, is important to understand their role. We focused on Hco-Pgp-13 since its ortholog in *C. elegans* is expressed in the nematode amphids, the strategic organs controlling chemotaxis, and for which a defect is associated with IVM resistance (Urdaneta-Marquez et al., 2014; Menez et al., 2016). Our overall objective was to characterize Hco-Pgp-13 and determine whether it could interact with drugs in order to predict its capacity to transport anthelmintics. Our data strongly support that Hco-Pgp-13 specifically interacts with IVM with high affinity, and may thus actively transport IVM and protect sensitive nematode tissues.

4.1. Topology and 3D structural models of Hco-Pgp-13

We first corrected the predicted *Hco-pgp-13* cDNA from the *H. contortus* genome (Laing et al., 2013) by identifying a misalignment of contigs due to a 30-nucleotide repeat in the previously published genomic sequence, absent in the full-length amplified cDNA. In addition, 90 single nucleotide polymorphisms (SNPs) were found in the amplified cDNA, similar to the 2.3% frequency of SNPs reported in different *H. contortus* populations. Based on the corrected sequence (GenBank No. KX844966), the full-length cDNA allowed prediction of a protein containing 1137 amino acids (MW 146 kDa), with typical domain arrangement of full-size ABC proteins, including 2 TMDs, and 2 NBDs containing the ABC transporter family consensus motifs, consistent with a primary active transporter. Hco-Pgp-13 shared close similarities with Cel-Pgp-12, Cel-Pgp-13 and Cel-Pgp-14, suggesting these proteins are orthologs between the two nematode species, possibly sharing some functional homologies.

Since the TMDs of Hco-Pgp-13 also share high sequence homology with the TMDs of Cel-Pgp-1 (54% similarity by BlastP), we generated 3D structures of Hco-Pgp-13 by homology modeling using the Cel-Pgp-1 crystal structure 4F4C (Jin et al., 2012), as template. Two model proteins Hco-Pgp-13_04 and Hco-Pgp-13_52 were selected according to their similarly high quality scores for several parameters (Table S2). They were both organized into two halves containing each six TM helices, but they presented an unusual supplementary transmembrane hairpin TMa-b at the N-terminus. For both models, 80% of hotspots residues, involved in drug binding in mammalian Pgps (Table S3), were detected and pointed towards the inner chamber lined by the TMDs. Nineteen percent of them were conserved, in terms of their nature, slightly below the 26% of hotspots residues conserved in Cel-Pgp-1 (David et al., 2016) as compared with mammalian Pgps. These data suggest that the overall protein topology of the inner chamber of Hco-Pgp-13 is consistent with a multispecific drug recognition site compatible with a multidrug transport function. However, only a small number of ABC proteins are endowed with a multidrug recognition capacity, and this raises the question of ligands interacting with Hco-Pgp-13.

4.2. High-affinity interaction of Hco-Pgp-13 with ACD and IVM

To study the ability of two toxins, ACD and IVM, to bind to Hco-Pgp-13, we characterized the putative binding sites *in silico*, by docking the two drugs on the two homology models described above. Allowing AutoDock 4 to “challenge” two different protein conformations with a semi-flexible docking strategy gave it the opportunity to explore a larger conformational space of the protein, which could simulate, to some extent, a flexible docking calculation strategy. The two conformations may reflect a preexisting equilibrium of two pools of proteins which may be stabilized upon ligand binding as the result of the movement of interacting residues or various membrane domains (Pike, 2004; Andre et al., 2008). ACD was chosen because this drug has been reported to strongly stimulate the ATPase activity of Cel-Pgp-1 (Jin et al., 2012) and to interact with the Cel-Pgp-1 binding pocket *in silico*, having the highest affinity among all tested ligands (David et al., 2016). We found that ACD and IVM both bound with high affinity in the inner chamber, revealing they are ligands of Hco-Pgp-13. The large ligand ACD (1255 Da) bound in the chamber from the cytoplasmic opening to the transmembrane inner core of the protein, whatever the protein model, while IVM (875 Da) presented a dual binding site, depending on the conformation of the protein. One of the binding sites of IVM substantially overlapped that of ACD in one protein model (_04), whereas it was deeper in the inner chamber and only partially overlapped the binding site of ACD in the other protein conformation (_52). The data revealed that the affinity of the binding site for a given ligand may depend on the conformation of the protein. Each ligand is expected to stabilize the lower energy conformation state of the formed complex. ACD seems to bind preferentially to the Hco-Pgp-13_04 conformation, whereas IVM has a higher affinity for the Hco-Pgp-13_52 conformation. In other words, the two built structural models are not “alternative” models, but are complementary conformations describing a preexisting dynamic transconformation equilibrium contributing to the specific affinity recognition of different ligands. The docking approach also provided important insights into drug interacting residues of the Hco-Pgp-13 binding pocket. Several residues formed H-bonds, among them, E21, L365, M1032 are common for ACD and IVM binding. In addition, several amino acids also aligned to hotspot residues on mammalian Pgp, suggesting that the inner chamber of Hco-Pgp-13 could form a binding domain competent for recognizing transport substrates of unrelated chemicals.

The ability to bind ACD and IVM was confirmed *in vitro* by

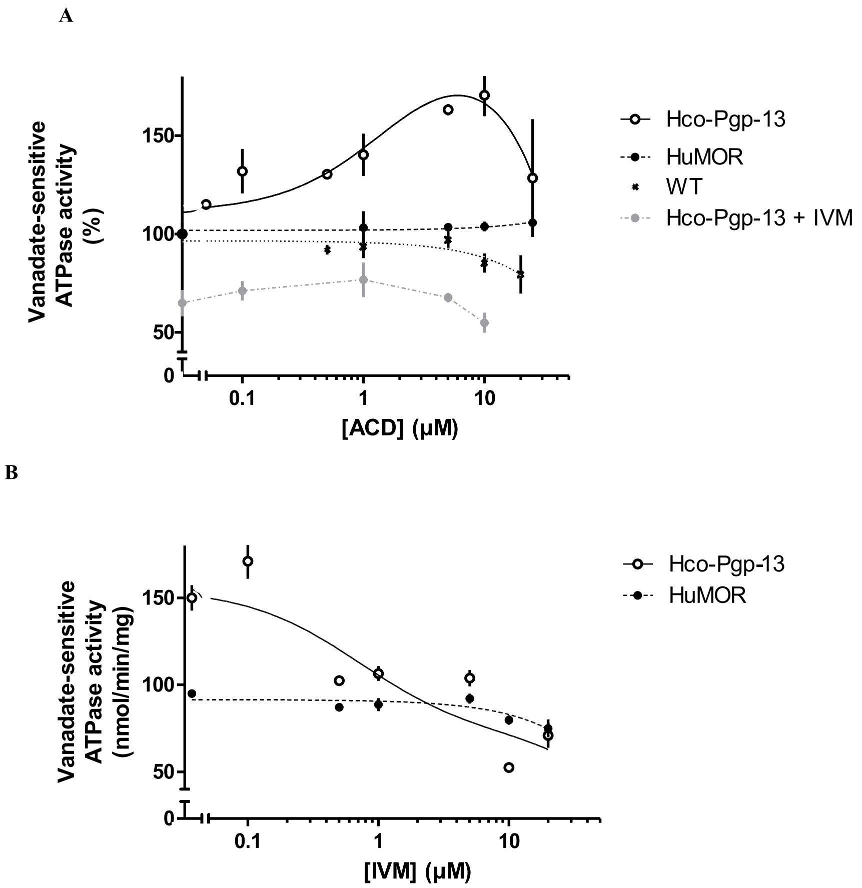

Fig. 4. Modulation of the ATPase activity of Hco-Pgp-13 by actinomycin D and ivermectin. Vanadate-sensitive ATPase activity was measured on freshly prepared membranes from either untransfected *P. pastoris* (wildtype (WT); black cross), or *P. pastoris* transfected with pPICZ-HuMOR-cmyc-his-tag vector (HuMOR; black circles) or with pPICZ-*Hco-Pgp-13*-cmyc-his-tag vector (Hco-Pgp-13; white circles), at 37 °C, as a function of ACD concentration in the absence (white and black symbols) or presence (grey circles) of 5 µM IVM (A) or IVM concentration (B). In Panel A, the vanadate-sensitive activity, measured as described in Material and Methods, was normalized to the control activity determined without drug for the same strain. The data are the mean ± SD of triplicates made on two or three independent experiments carried out on HuMOR, Hco-Pgp-13 and WT membranes, respectively. The lines are fits using GraphPad PRISM.

measuring modulation of ATPase activity in cell membranes expressing Hco-Pgp-13. ACD specifically stimulated the basal Hco-Pgp-13 ATPase activity. The ACD half-activating concentration for Hco-Pgp-13 stimulation ($EC_{50} = 0.6–1\ \mu M$) was higher than that for Cel-Pgp-1 ($EC_{50} \approx 0.05\ \mu M$) (Jin et al., 2012); however, the experimental conditions differed between the two sets of measurements. The *in silico* docking of ACD on Cel-Pgp-1 showed that it interacts with a comparable binding energy as with Hco-Pgp-13, at a similar site located at the cytosolic opening of the inner chamber (David et al. to be submitted). Since ATP hydrolysis is required to drive active translocation across cell membranes, our data indicate that ACD is transported by Hco-Pgp-13 similarly to Cel-Pgp-1. Interestingly, in the absence of any added drug, a higher ATPase activity in the membranes of yeast expressing Hco-Pgp-13, as compared to that of the control membranes, suggests that Hco-Pgp-13 can transport some substrates present in the membranes.

IVM inhibited the basal Hco-Pgp-13 ATPase activity in a concentration dependent-manner with an apparent half-maximal inhibitory concentration of 0.5–0.7 µM, which suggests that it can specifically bind to Hco-Pgp-13. In addition, the total inhibition of the ACD-stimulated ATPase activity by 5 µM IVM is consistent with binding to the same site as that inhibiting the basal activity, which was half-saturated at ≈ 0.6 µM. The consistency between the two effects of IVM strongly supports that it binds to a specific site on Hco-Pgp-13 with a sub-micromolar affinity. It is noteworthy that it has also been reported that the interaction of IVM with mammalian Pgp induces an inhibition of its basal ATPase activity (Lespine et al., 2007). This inhibition was explained as the consequence of a slower translocation of IVM than that of endogenous substrates, including cholesterol (Garrigues et al., 2002).

In silico docking calculations indicated a lower affinity for IVM than ACD for its specific binding site (binding energy of -12,8 *vs* -16,0 kcal/mol, respectively). In contrast, *in vitro* experiments showed similar apparent affinities, in the 0.5 to 1 µM range. If we consider that Hco-Pgp-13 behaves like mammalian Pgp and, in its open inward-facing conformation, binds its hydrophobic substrates from within the membrane (Sharom, 2008; Eckford and Sharom, 2009), the *in vitro* measured affinity of an amphiphilic/hydrophobic ligand will be a combination of its membrane partition coefficient and the "theoretical affinity" with its specific binding site. Since IVM is much more hydrophobic than ACD, it will be more concentrated within the membrane, hence the *in silico* data can be quantitatively reconciled by considering that the higher membrane partition coefficient of IVM compensates for its lower theoretical affinity. *In silico* calculations also showed that IVM was docked, for the more stable conformation, in the deepest part of the inner chamber of the protein, which was in agreement with the previously determined *in silico* docking of IVM on Cel-Pgp-1 (David et al., 2016). Finally the *in silico* data predict that IVM should inhibit ACD-induced ATPase stimulation, due to the partial overlap of their drug binding sites, and this was observed *in vitro*.

4.3. Tissue immunolocalization of Hco-Pgp-13

It was of interest to determine in which tissues of *H. contortus* Hco-Pgp-13 is expressed. Hco-Pgp-13 was found in the digestive apparatus, which can be an entry route for xenobiotics; in the seam cells lining the excretory canals, involved in xenobiotic elimination; and in head neurons, possibly the amphids, which may play a role in the access of ML to the targets responsible for lethal anthelmintic effects on nematodes. Since shortening of amphidial dentrites is associated with resistance to IVM in *H. contortus* and in *C. elegans* (Freeman et al., 2003; Urdaneta-Marquez et al., 2014; Menez et al., 2016), the staining of adult head neurons matching the amphids suggests a link for Hco-Pgp-13 involvement in IVM resistance. The pharyngeal structures were also stained, and may correspond with the neurons innervating the pharynx. Since a major effect of ML on nematodes is paralysis of the pharyngeal

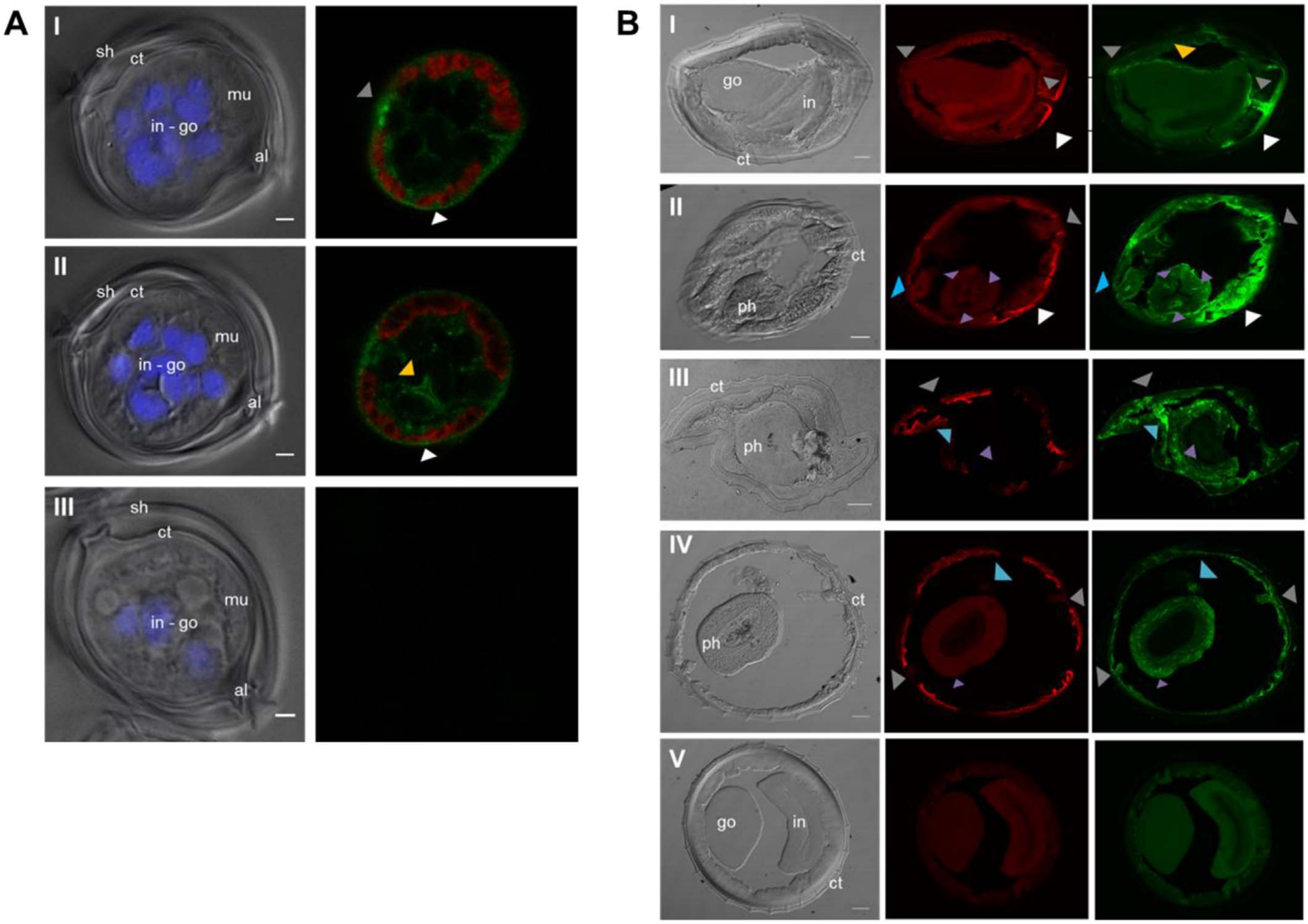

Fig. 5. Immunolocalization of Hco-Pgp-13 in *Haemonchus contortus* L3 larvae (A) and adult (B). A. Left panel: differential interference contrast (DIC) image and DAPI signal superimposed; right panel: myosin and Hco-Pgp-13 staining superimposed. **I** and **II:** Different Z-stacks of one slice in the mid-body observed after incubation of primary and secondary antibodies. **III:** Slice in the mid-body observed with no primary antibody incubation. All slices were incubated with DAPI, and numerous nuclei are observed in the gonad and intestine in development and not well distinguishable. sh = supplementary sheath of the L3 stage larvae, ct = cuticle, al = alae, in = intestine, go = gonad, mu = muscle. White arrow: hypodermis, grey arrow: seam cell, yellow arrow: epithelial cells of the gonad or intestine. Scale bar = 2 μm. **B.** Left panel: DIC image; middle panel, myosin staining; right panel, Hco-Pgp-13 staining. **I:** Slice in the mid-body of a male parasite. **II:** Slice in the anterior region of the pharynx (procorpus). **III:** Section in the mid-region of the pharynx (metacorpus). **IV:** Section in the posterior region of the pharynx (terminal bulb). **I**–**IV:** Incubation of primary and secondary antibodies. **V:** No primary antibody incubation. ct = cuticle, ph = pharynx, go = gonad, in = intestine. White arrow: hypodermis, grey arrow: seam cell-excretory cell, blue arrow: neuronal structures, purple arrow: pharyngeal glands, yellow arrow: gonad. Scale bar = 20 μm. (For interpretation of the references to colour in this figure legend, the reader is referred to the Web version of this article.)

muscles, Hco-Pgp-13 expression in pharyngeal neurons might protect worms from IVM effects. The expression of Hco-Pgp-13 in the epithelial cells of the larvae and adult gonad resembled previous finding of Hco-Pgp-9.1 expression in the uterus (Godoy et al., 2016), and an involvement in reducing toxic compounds reaching embryos, as was shown in *C. elegans* (Brinke et al., 2013) and mammalian placental tissue (Nakamura et al., 1997; Kolwankar et al., 2005).

The Hco-Pgp-13 expression matches the global transcript localization of all of its closest ortholog genes in *C. elegans* with *Cel-Pgp-12* expressed in the excretory cell, *Cel-Pgp-13* in the posterior intestine and amphids of adults, *Cel-Pgp-14* in the anterior region and first bulb of the pharynx in the adults and larvae, and *Cel-Pgp-15* in the adult head and tail neurons, and in the embryo (Zhao et al., 2004). Interestingly, the three genes *Cel-Pgp-12*, *Cel-Pgp-13*, *Cel-Pgp-14*, together with the pseudogene *Cel-Pgp-15*, form a cluster of tandemly duplicated genes on chromosome X of *C. elegans* (Zhao et al., 2004). Since, *H. contortus* lacks the Pgp-12 and Pgp-14 proteins, the broad localization observed here for Hco-Pgp-13 may cover all the functions ensured in *C. elegans* by its three ortholog Pgps.

This study represents the first structural and functional analysis of a parasitic nematode Pgp, describing its molecular interaction with two important drugs, ACD and IVM. This provides critical information on the protective function of Hco-Pgp-13 against toxicity of IVM and other drugs. Its location, mainly in strategic tissues of *H. contortus,* underlines the importance of this transporter and its possible role in anthelmintic resistance.

Acknowledgements

The authors thank Lea Lasvaux and Melanie Gentil for their help in the ATPase activity measurements and Western-blot experiments, Thierry Gauthier for providing his expertise and access to confocal microscope. We also thank Fabien Jourdan and Clément Frainay for technical support with bioinformatics experiments and the Genotoul Bioinformatics hardware infrastructure that was used for computing. We also acknowledge the staff of the computing facility of the Biology division of CEA/DRF/GIPSI at Saclay for help and access to the national cluster Gabriel. This work was supported by the Natural Sciences and Engineering Research Council of Canada (grant No. RGPIN/2777-2012), the FRQNT Centre for Host-Parasite Interactions, Quebec, and EMIDA ERA-NET project CARES n 11-EMID-003-02.

Appendix A. Supplementary data

Supplementary data related to this article can be found at http://dx.doi.org/10.1016/j.ijpddr.2018.02.001.

References

Aller, S.G., Yu, J., Ward, A., Weng, Y., Chittaboina, S., Zhuo, R., Chang, G., 2009. Structure of P-glycoprotein reveals a molecular basis for poly-specific drug binding. Science 323, 1718–1722.

Andre, A., Gaibelet, G., Le Guyader, L., Welby, M., Lopez, A., Lebrun, C., 2008. Membrane partitioning of various delta-opioid receptor forms before and after agonist activations: the effect of cholesterol. Biochim. Biophys. Acta 1778, 1483–1492.

Ardelli, B.F., Prichard, R.K., 2013. Inhibition of P-glycoprotein enhances sensitivity of Caenorhabditis elegans to ivermectin. Vet. Parasitol. 191, 264–275.

Bartley, D.J., McAllister, H., Bartley, Y., Dupuy, J., Ménez, C., Alvinerie, M., Lespine, A., 2009. P-glycoprotein interfering agents potentiate ivermectin susceptibility in ivermectin sensitive and resistant isolates of Teladorsagia circumcincta and Haemonchus contortus. Parasitology 136, 1081–1088.

Benkert, P., Tosatto, S.C.E., Schomburg, D., 2008. QMEAN: a comprehensive scoring function for model quality assessment. Protein. Struct. Funct. Bioinf. 71, 261–277.

Benkert, P., Künzli, M., Schwede, T., 2009. QMEAN server for protein model quality estimation. Nucleic Acids Res. 37 (Suppl. 2), 510–514.

Bessadok, A., Garcia, E., Jacquet, H., Martin, S., Garrigues, A., Loiseau, N., Vivaudou, M., 2011. Recognition of sulfonylurea receptor (ABCC8/9) ligands by the multidrug resistance transporter P-glycoprotein (ABCB1): functional similarities based on common structural features between two multispecific ABC proteins. J. Biol. Chem. 286, 3552–3569.

Blaxter, M., Liu, L., 1996. Nematode spliced leaders-ubiquity, evolution and utility. Int. J. Parasitol. 26, 1025–1033.

Brinke, M., Heininger, P., Traunspurger, W., 2013. Effects of a bioassay-derived ivermectin lowest observed effect concentration on life-cycle traits of the nematode Caenorhabditis elegans. Ecotoxicology 22, 148–155.

Campbell, W.C., 2016. Ivermectin: a reflection on simplicity (nobel lecture). Angew. Chem. Int. Ed. Engl. 55, 10184–10189.

Corpet, F., 1988. Multiple sequence alignment with hierarchical clustering. Nucleic Acids Res. 16, 10881–10890.

David, M.A., Orlowski, S., Prichard, R.K., Hashem, S., Andre, F., Lespine, A., 2016. In silico analysis of the binding of anthelmintics to Caenorhabditis elegans P-glycoprotein 1. Int. J. Parasitol. Drugs Drug Res. 6, 299–313.

Eckford, P.D.W., Sharom, F., 2009. ABC efflux pump-based resistance to chemotherapy drugs. Chem. Rev. 109, 2989–3011.

Edgar, R.C., 2004a. MUSCLE: a multiple sequence alignment method with reduced time and space complexity. BMC Bioinf. 5, 113.

Edgar, R.C., 2004b. MUSCLE: multiple sequence alignment with high accuracy and high throughput. Nucleic Acids Res. 32, 1792–1797.

Freeman, A.S., Nghiem, C., Li, J., Ashton, F.T., Guerrero, J., Shoop, W.L., Schad, G.A., 2003. Amphidial structure of ivermectin-resistant and susceptible laboratory and field strains of Haemonchus contortus. Vet. Parasitol. 110, 217–226.

Gallagher, S.R., 2016. One-dimensional SDS gel electrophoresis of proteins. Curr. Protoc. Immunol 1–44 Chapter 10: Unit 10.1.

Garrigues, A., Loiseau, N., Delaforge, M., Ferté, J., Garrigos, M., André, F., Orlowski, S., 2002. Characterization of two pharmacophores on the multidrug transporter P-glycoprotein. Mol. Pharmacol. 62, 288–1298.

Godoy, P., Lian, J., Beech, R.N., Prichard, R.K., 2015a. Haemonchus contortus P-glycoprotein-2: in situ localisation and characterisation of macrocyclic lactone transport. Int. J. Parasitol. 45, 85–93.

Godoy, P., Che, H., Beech, R.N., Prichard, R.K., 2015b. Characterization of Haemonchus contortus P-glycoprotein-16 and its interaction with the macrocyclic lactone anthelmintics. Mol. Biochem. Parasitol. 204, 11–15.

Godoy, P., Che, H., Beech, R.N., Prichard, R.K., 2016. Characterisation of P-glycoprotein-9.1 in Haemonchus contortus. Parasit. Vectors 9, 52.

Hewitt, E.W., Lehner, P.J., 2003. The ABC-transporter signature motif is required for peptide translocation but not peptide binding by TAP. Eur. J. Immunol. 33, 422–427.

James, C.E., Davey, M.W., 2009. Increased expression of ABC transport proteins is associated with ivermectin resistance in the model nematode Caenorhabditis elegans. Int. J. Parasitol. 39, 213–220.

Janssen, I.J., Krucken, J., Demeler, J., von Samson-Himmelstjerna, G., 2013a. *Caenorhabditis elegans*: modest increase of susceptibility to ivermectin in individual P-glycoprotein loss-of-function strains. Exp. Parasitol. 134, 171–177.

Janssen, I.J., Krücken, J., Demeler, J., Basiaga, M., Kornaś, S., von Samson-Himmelstjerna, G., 2013b. Genetic variants and increased expression of Parascaris equorum P-glycoprotein-11 in populations with decreased ivermectin susceptibility. PLoS One 8, e61635.

Janssen, I.J., Krucken, J., Demeler, J., von Samson-Himmelstjerna, G., 2015. Transgenically expressed Parascaris P-glycoprotein-11 can modulate ivermectin susceptibility in Caenorhabditis elegans. Int. J. Parasitol. Drugs Drug Resist. 5, 44–47.

Jin, M.S., Oldham, M.L., Zhang, J., Chen, Q., 2012. Crystal structure of the multidrug transporter P-glycoprotein from Caenorhabditis elegans. Nature 490, 566–569.

Jones, P.M., George, A.M., 2005. Multidrug resistance in parasites: ABC transporters, P-glycoproteins and molecular modelling. Int. J. Parasitol. 35, 555–566.

Kaplan, R.M., Vidyashankar, A.N., 2012. An inconvenient truth: global worming and anthelmintic resistance. Vet. Parasitol. 186, 70–78.

Kaschny, M., Demeler, J., Janssen, I.J.I., Kuzmina, T.A., Besognet, B., Kanellos, T., Kerboeuf, T., von Samson-Himmelstjerna, G., Krücken, J., 2015. Macrocyclic lactones differ in interaction with recombinant P-glycoprotein 9 of the parasitic nematode Cylicocylus elongatus and ketoconazole in a yeast growth assay. PLoS Pathog. 11 e1004781.

Koenderink, J.B., Kavishe, R.A., Rijpma, F.G., Russel, S.R., 2010. The ABCs of multidrug resistance in malaria. Trends Parasitol. 26, 440–446.

Kolwankar, D., Glover, D.D., Ware, T.S., Tracy, J.A., 2005. Expression and function of ABCB1 and ABCG2 in human placental tissue. Drug Metab. Dispos. 33, 524–529.

Lage, H., 2003. ABC-transporters: implications on drug resistance from microorganisms to human cancers. Int. J. Antimicrob. Agents 22, 188–199.

Laing, R., Kikuchi, T., Martinelli, A., Tsai, I.J., Beech, R.N., Redman, E., Holroyd, N., Bartley, D.J., Beasley, H., Britton, C., Curran, D., Devaney, E., Gilabert, A., Hunt, M., Jackson, F., Johnston, S.L., Kryukov, I., Li, K., Morrison, A.A., Reid, A.J., Sargison, N., Saunders, G.I., Wasmuth, J.D., Wolstenholme, A., Berriman, M., Gilleard, J.S., Cotton, J.A., 2013. The genome and transcriptome of Haemonchus contortus, a key model parasite for drug and vaccine discovery. Genome Biol. 14 R88.

Lespine, A., Martin, S., Dupuy, J., Roulet, A., Pineau, T., Orlowski, S., Alvinerie, M., 2007. Interaction of macrocyclic lactones with P-glycoprotein: structure-affinity relationship. Eur. J. Pharm. Sci. 30, 84–94.

Lespine, A., Menez, C., Bourguinat, C., Prichard, R.K., 2012. P-glycoproteins and other multidrug resistance transporters in the pharmacology of anthelmintics: prospects for reversing transport-dependent anthelmintic resistance. Int. J. Parasitol. Drugs Drug Resist. 2, 58–75.

Li, J., Jaimes, K.F., Aller, S.G., 2013. Refined structures of mouse P-glycoprotein. Protein. Sci. 23, 34–46.

Loo, T.W., Clarke, D.M., 2001. Defining the drug-binding site in the human multidrug resistance P-glycoprotein using a methanethiosulfonate analog of verapamil, MTS-verapamil. J. Biol. Chem. 276, 14972–14979.

Loo, T.W., Clarke, D.M., 2002. Location of the rhodamine-binding site in the human multidrug resistance P-glycoprotein. J. Biol. Chem. 277, 44332–44338.

Loo, T.W., Bartlett, M.C., Clarke, D.M., 2006a. Transmembrane segment 1 of human P-glycoprotein contributes to the drug-binding pocket. Biochem. J. 396, 537–545.

Loo, T.W., Bartlett, M.C., Clarke, D.M., 2006b. Transmembrane segment 7 of human P-glycoprotein contributes to the drug-binding pocket. Biochem. J. 399, 351–359.

Mani, T., Bourguinat, C., Keller, K., Ashraf, S., Blagburn, B., Prichard, R.K., 2016. Interaction of macrocyclic lactones with a Dirofilaria immitis P-glycoprotein. Int. J. Parasitol. 46, 631–640.

Menez, C., Alberich, M., Kansoh, D., Blanchard, A., Lespine, A., 2016. Acquired tolerance to ivermectin and moxidectin after drug selection pressure in the nematode Caenorhabditis elegans. Antimicrob. Agents Chemother. 60, 4809–4819.

Morris, G.M., Goodsell, D.S., Halliday, R.S., Huey, R., Hart, W.E., Belew, R.K., Olson, A.J., 1998. Automated docking using lamarckian genetic algorithm and an empirical binding free energy function. J. Comput. Chem. 19, 1639–1662.

Morris, G.M., Huey, R., Lindstrom, W., Sanner, M.F., Belew, R.K., Goodsell, D.S., Olson, A.J., 2009. AutoDock4 and AutoDockTools4: automated docking with selective receptor flexibility. J. Comput. Chem. 30, 2785–2791.

Nakamura, Y., Ikeda, S., Furukawa, T., Sumizawa, T., Tani, A., Akiyama, S., Nagata, Y., 1997. Function of P-glycoprotein expressed in placenta and mole. Biochem. Biophys. Res. Commun. 235, 849–853.

Omasits, U., Ahrens, C.H., Muller, S., Wollscheid, B., 2014. Protter: interactive protein feature visualization and integration with experimental proteomic data. Bioinformatics 30, 884–886.

Pike, L.J., 2004. Lipid rafts: heterogeneity on the high seas. Biochem. J. 378, 281–292.

Pouliot, J.F., L'Heureux, F., Liu, Z., Prichard, R.K., Georges, E., 1997. Reversal of P-glycoprotein-associated multidrug resistance by ivermectin. Biochem. Pharmacol. 53, 17–25.

Ranjan, S., Wang, G.T., Hirschlein, C., Simkins, K.L., 2002. Selection for resistance to macrocyclic lactones by Haemonchus contortus in sheep. Vet. Parasitol. 103, 109–117.

Roulet, A., Puel, O., Gesta, S., Lepage, J.F., Drag, M., Soll, M., Alvinerie, M., Pineau, T., 2003. MDR1-deficient genotype in Collie dogs hypersensitive to the P-glycoprotein substrate ivermectin. Eur. J. Pharmacol. 460, 85–91.

Sali, A., Blundell, T.L., 1993. Comparative protein modelling by satisfaction of spatial restraints. J. Mol. Biol. 234, 779–815.

Sarkadi, B., Price, E.M., Boucher, R.C., Germann, U.A., Scarborough, G.A., 1992. Expression of the human multidrug resistance cDNA in insect cells generates a high activity drug-stimulated membrane ATPase. J. Biol. Chem. 267, 4854–4858.

Sarramegna, V., Muller, I., Mousseau, G., Froment, C., Monsarrat, B., Milon, A., Talmont, F., 2005. Solubilization, purification, and mass spectrometry analysis of the human mu-opioid receptor expressed in Pichia pastoris. Protein Expr. Purif. 43, 85–93.

Schinkel, A.H., Smit, J.J.M., van Tellingen, O., Beijnen, J.H., Wagenaar, E., van Deemter, L., Mol, C.A., van der Valk, M.A., Robanus-Maandag, E.C., te Riele, H.P., et al., 1994. Disruption of the mouse mdr1a P-glycoprotein gene leads to a deficiency in the blood-brain barrier and to increased sensitivity to drugs. Cell 77, 491–502.

Sharom, F.J., 2008. ABC multidrug transporters: structure, function and role in chemoresistance. Pharmacogenomics 9, 105–127.

Shilling, R.A., Venter, H., Velamakanni, S., Bapna, A., Woebking, B., Shahi, S., van Veen, H.W., 2006. New light on multidrug binding by an ATP-binding-cassette transporter. Trends Pharmacol. Sci. 27, 195–203.

Sippl, M.J., 1993. Recognition of errors in three-dimensional structures of proteins.

Proteins 17, 355–362.

Urdaneta-Marquez, L., Bae, S.H., Janukavicius, P., Beech, R., Dent, J., Prichard, R., 2014. A dyf-7 haplotype causes sensory neuron defects and is associated with macrocyclic lactone resistance worldwide in the nematode parasite Haemonchus contortus. Int. J. Parasitol. 44, 1063–1071.

Webb, B., Sali, A., 2014. Comparative protein structure modeling using MODELLER. Curr. Protoc. Bioinformatics 47 (5), 1–32 6.

Wiederstein, M., Sippl, M.J., 2007. ProSA-web: interactive web service for the recognition of errors in three-dimensional structures of proteins. Nucleic Acids Res. 35, W407–W410.

Willard, L., Ranjan, A., Zhang, H., Monzavi, H., Boyko, R.F., Sykes, B.D., Wishart, D.S., 2003. VADAR: a web server for quantitative evaluation of protein structure quality. Nucleic Acids Res. 31, 3316–3319.

Ōmura, S.A., 2016. Splendid gift from the earth: the origins and impact of the avermectins (nobel lecture). Angew. Chem. Int. Ed. 55, 10190–10209.

Zhao, Z., Sheps, J.A., Ling, V., Fang, L.L., Baillie, D.L., 2004. Expression analysis of ABC transporters reveals differential functions of tandemly duplicated genes in Caenorhabditis elegans. J. Mol. Biol. 344, 409–417.